High-resolution surface-wave-constrained mapping of sparse dynamic cone penetrometer tests

Ao Wang, Fayçal Rejiba, Ludovic Bodet, Cécile Finco, Cyrille Fauchard

High-Resolution Surface-Wave-Constrained Mapping of Sparse Dynamic Cone Penetrometer tests

Ao Wang*[1], Fayçal Rejiba[2], Ludovic Bodet[2], Cécile Finco[1], and Cyrille Fauchard[1]

[1]Cerema, Research Team ENDSUM , F-76121, Le-Grand-Quevilly, France

[2]Sorbonne Universite, CNRS, EPHE, UMR 7619 METIS, 75005, Paris, France

November 2023

Short running title (50 characters max): Mesoscale SW-Constrained Mapping of DCP

Acknowledgements

This work was supported by the European Office of Aerospace Research & Development (EOARD) with Grant FA9550-19-1-7041 and by the University of

*Corresponding author. Email: ao.wang@cerema.fr

Dayton Research Institute contract RSC18040 in support of the US Air Force Prime Contract Number FA8650-18-C-2808. The authors would like to thank the technical team of Cerema Normandie Centre in Rouen, France, for their part in the test site construction and their ongoing assistance with test site maintenance and measurements. The authors also express their sincere gratitude to Mr. Emmanuel Delaure, Pr. Pierre Delage and Pr. Yu Jun Cui of the Navier laboratory (UMR 8205) in Marne-la-Vallée, France, for their help and advice in the design and construction of the test site and in laboratory measurements of the samples. Sincere gratitude is equally expressed to Dr. Cyril Schamper and Mr. Ayoub Saydy for their help with exhaustive DCP tests and geophysical measurements at the test site. Finally, the authors would like to thank Dr. Luis Henrique Cavalcante Fraga, for all of the revisions and suggestions that he made during his time as a post-doctoral fellow working on this project.

Abstract

The Dynamic Cone Penetrometer (DCP) provides local soil resistance information. The difference in the vertical and horizontal data resolution (centimetric vs. multi-metric) makes it difficult to spatialize the DCP data directly. This study uses high-resolution V_s section, extracted by the seismic surface-wave method, as the auxiliary and physical constrain for mapping the DCP Index ($DCPI$). Geostatistical formalism (kriging and cokriging) is used. The associated measurement error of the seismic surface-wave data is also included in the cokriging system, i.e. the CoKriging with Variance of Measurement Error (CKVME). The proposed methods are validated for the first time on a test site designed and constructed for this study, with known geotechnical perspectives. Seismic and high-intensity DCP campaigns were performed on the test site. The results show that with the decimating number of DCP soundings, the kriging

approach is no more capable to estimate the lateral variation in the test site, and the RMSE value of the kriging section is increased by 87%. With the help of V_s sections constraining the lateral variability model, the RMSE values of the cokriging and the CKVME sections are increased by 25% and 17%.

Keywords: cone-penetration-test, geotechnical, inversion, shallow subsurface, surface wave

Data Availability Statement: The data that support the findings of this study are available from the corresponding author upon reasonable request.

Conflict of interest: The authors declare to have no conflict of interest, nor financial interests to report upon the submission and publication of the research paper.

1 Introduction

The bearing capacity is the main parameter to assess in order to design stable and safe structures. Among numerous *in situ* test to estimate this parameter directly or indirectly, the Dynamic Cone Penetrometer (DCP) is the standardized technique the most used for the civil engineering structure design, e.g. Nazarian et al. (2000); Mohammadi et al. (2008). The common application of DCP is to convert the raw penetration depth of the tip after each blow, i.e. DCP Index ($DCPI$), into bearing capacity or resistance ratio through empirical formulas (Porter, 1939). As every *in situ* geotechnical tests, a DCP sounding provides local information, and its implementation at meso scale faces the difficulty of combining good resolution and continuous mapping; currently, there is no way to map the bearing capacity directly and continuously other than by implementing intensive and dense DCP campaigns (Sastre Jurado et al., 2021).

Many studies have been devoted to the combination of geotechnical and geophysical methods for site scale surveys (Cosenza et al., 2006; Haines et al., 2009; Masoli et al., 2020) benefiting from the capacity of geophysical methods to provide physical properties of the subsurface over large areas. The S-wave velocity (V_s) cross-section extracted by the multi-channel analysis of seismic surface-wave methods (MASW) (Hayashi and Suzuki, 2004; Pasquet and Bodet, 2017) is particularly interesting in this context as it is directly connected to the ground mechanical properties (Mayne and Rix, 1995; Mola-Abasi et al., 2015; Adama et al., 2023). Examples can be found by combining the cone tip resistance data obtained during CPT (Cone Penetration Test) and V_s data extracted by MASW in Xu et al. (2022) with data fusion methods, and in Huang et al. (2018) with Bayesian statistical methods. In this study, the geostatistical approaches (Chiles and Delfiner, 2009) are applied for the mapping of $DCPI$ data with the help of MASW. Before applying geostatistical analyses on the MASW and DCP data, several issues must be addressed.

A first issue concerns the requirement to have a comparable resolution in both vertical and horizontal directions between DCP and seismic measurements because they need to be resampled on the same grid. DCP soundings are much more densely sampled vertically than horizontally (centimetric vs. multi-metric), while MASW surveys have a resolution that degrades rapidly with depth and integrate the spread corresponding to the length of the setup due to the one dimensional assumption for the inversion model (Socco and Strobbia, 2004; Bodet et al., 2005). A second issue concerns the difficulty to describe the very near surface at a sub-decimetric resolution while using classical geophones and seismic sources. This is due to the requirement of measuring high frequency content emitted from the source in addition to minimum distance between geophones, which leads to an inevitable shadow zones from the surface (Socco and

Strobbia, 2004). The sub-decimetric resolution is considered as the minimum realistic objective to reach the vertical resolution of the DCP. Consequently the errors due either to the geometrical setup or to external noise should be included as constraints into the mapping process of DCP.

The main objective of this study is therefore to test a protocol for mapping a set of sparse DCP soundings using data from MASW surveys as auxiliary and physical constraints. The ability to map DCP data under seismic constraints will be specifically evaluated, particularly in the case with very few DCP available soundings. In the present study, a test site was built with a silty-clay material and a lateral gradient of compaction, on a rigid natural ground constituted of historical gravel fill. The size of the test site, $29 \times 5m^2$, was chosen to be sufficient to carry out realistic classical high-resolution seismic survey with standard seismic instruments.

In order to avoid introducing errors using empirical formulas, the $DCPI$ values instead of the bearing capacity or cone tip resistance are used for the mapping. Lateral and vertical mapping of $DCPI$ constrained by V_s is assessed using co-kriging (Goovaerts, 1998), which assesses and then uses the spatial correlation between different types of data through the cross-variogram once a common grid is defined. Vertically, the contribution of the MASW data in the geostatistical formalism is comparable to that of the DCP, owing to the smooth-model inversion based on the Non-Linear Least Square Method (NLLSM) (Feng and Sugiyama, 2001; Hayashi, 2008). But laterally, one can only use the *a priori* information provided by the inverted V_s profile to constraint the interpolation between DCP soundings. Moreover, the CoKriging with Variance of Measurement Error (CKVME) (Wackernagel, 2003; Christensen, 2011) is also applied in the proposed approach. The errors of the extracted V_s values are estimated for each profile and integrated into the cokriging formula. These errors include

the measurement errors due to the seismic set-ups and the external noise, as well as the uncertainties in the inversion model related to the sensitivity of the MASW approach.

2 Methods and material

2.1 Test site description

The test site was constructed in 2019 at Cerema (Centre for Studies on Risks, the Environment, Mobility, and Urban Planning) Normandie-Centre facilities, near Rouen, Normandie, France at position 358020E, 5472975N (the coordinate system is WGS84 UTM31N in meter). It was designed to have three distinct areas, named Area 1, Area 2, and Area 3, corresponding to three levels of compaction (Area 1>Area 2>Area 3, California Bearing Ratio between 3 and 10). Each area is $7\,m$ long, $5\,m$ wide, and $0.75\,m$ deep, and they are separated by two $4\,m$ long dead zones to allow landfill compactor to access the site during its construction (Fig. 1 (a) and (c)). The material used for the test site was a clayey-sandy silt of type A1 (French standard NF P11-300). Fig. 1 (d) gives the location of the DCP soundings and of the seismic profile for the surface-wave measurements. Three soil cores were extracted from the test site and one TDR (Time-Domain Reflectometer) sensor is buried in Area 3. Their locations are presented in Fig. 1 (d) and details on the measurements are available in Appendix A.

2.2 DCP measurements

DCP tests were acquired at the test site on a dense $50 \times 50\,cm^2$ grid in both X and Y directions ($X \in [0, 4.5]\,m$, $Y \in [0.3, 28.3]\,m$, Fig. 1 (c)). Kessler DCPs were used (Fig. 1 (b)). Each instrument has a standard hammer mass of

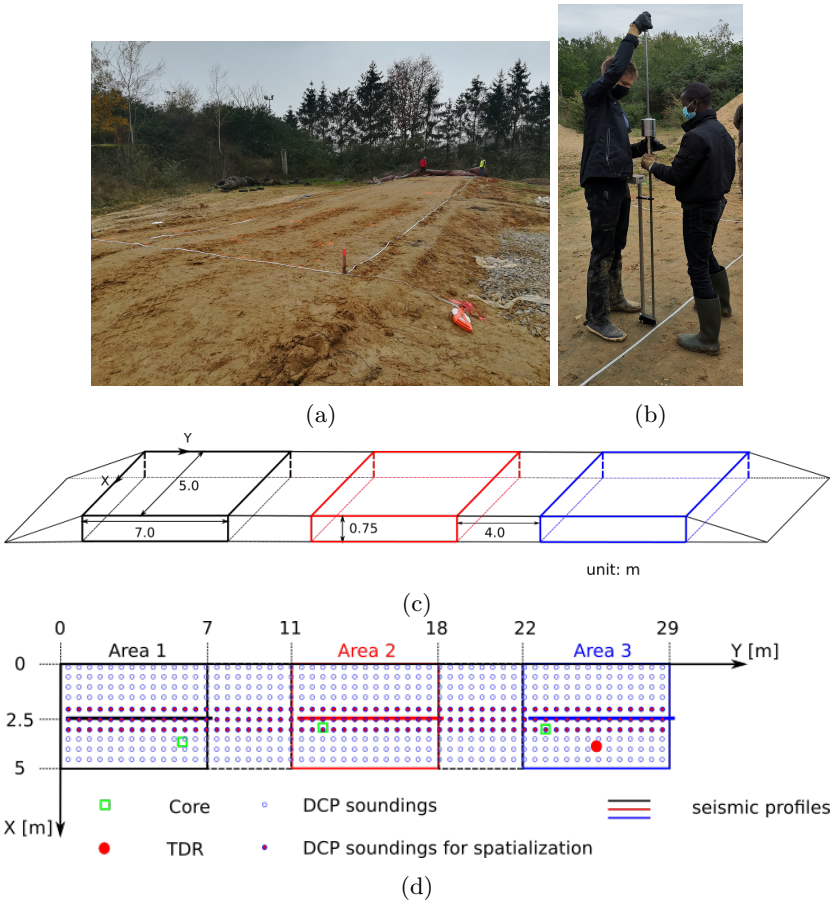

Figure 1: (a) Photograph of test site at CEREMA in Rouen, France. (b) Geotechnical campaign with Kessler DCP. (c) Schematic diagram of the test site with dimensions. Black: Area 1; red: Area 2; blue: Area 3. (d) Schematic of the DCP and seismic measurements.

$8\,kg$, and its free-fall of $57.5\,cm$ causes the tip of the DCP to penetrate the soil. More details of DCP designs, standards and applications can be found in ASTM D6951 (2009); Webster et al. (1992). The raw DCP data, i.e. $DCPI$, were used as proxy for the soil resistance in this study. Fig. 2 (a) shows the raw $DCPI$ values at the centerline of test site ($X = 2.5\,m$, 57 DCP soundings). Small values of $DCPI$ represents high bearing capacity or resistance of the soil, and vice versa. $DCPI$ variations can be observed inside each area in both the lateral (Y) and vertical (Z) directions. A layer of relatively low soil resistance exists at approximately $200-400\,mm$ in Area 1, and its thickness varies laterally. Area 2 also contains a layer of low resistance between $100-250\,mm$ and its position and thickness are constant across the area. Area 3 exhibits lateral variations, but its overall $DCPI$ values show a large difference from those of Area 1 and Area 2.

Fig. 2 (b) shows the mean and standard deviation values of $DCPI$ in each area (126 soundings in each area), as a function of depth. Among the three areas, Area 3 has the largest $DCPI$ values indicating the lowest soil resistance. Although the construction design aimed for a higher level of compaction in Area 1 than in Area 2, the raw $DCPI$ values show a high degree of similarity between them. Table 1 resumes the mean and standard deviation (STD) values of $DCPI$ in each of three areas. Area 3 has a mean value of $DCPI$ equal to $20\,mm/blow$ which is 1.5 times greater than that of Area 1 and Area 2, and the STD of $DCPI$ in Area 3 is more than double that of the other two zones, which is due to the significant difference in $DCPI$ at the test site and the natural ground interface.

The mean and STD values of the cumulative $DCPI$ were calculated for DCP soundings acquired in each area and are shown in Fig. 2 (c). The penetration rate of the DCP, i.e. the slope of each line, named S_{DCP} hereafter, is therefore a

	Mean $[mm/blow]$	Standard deviation $[mm/blow]$
Area 1	12	7
Area 2	13	8
Area 3	20	18

Table 1: Mean and standard deviation values of $DCPI$ for each area.

proxy for evaluating the soil resistance of each area. The Knee Point Detection (KPD) method (Satopaa et al., 2011) is applied on the penetration depth curve of DCP sounding in order to detect the "knee" of each DCP sounding where S_{DCP} flattens, i.e. the depth of test site. The estimated depths are presented in Fig. 2 (a) as red curve. The black curve is the depth measurement provided by Cerema technical team during the construction of test site. The difference between two curves is mainly due to the residual roughness and slight topographic variations of the ground base.

To compare DCP soundings with the seismic surface-wave profile and to reduce the impact of local anomalies, the mean values of the cumulative $DCPI$ at the centre and its adjacent lines ($X = 2.0\,m$, $2.5\,m$ and $3.0\,m$, Fig. 1 (d)) are calculated with a total number of 58 DCP soundings. The corresponding $DCPI$ values are are used in the following.

2.3 Surface-wave methods

2.3.1 Seismic data acquisition and processing

Three seismic profiles of identical spread lengths were acquired in the three areas on the central line at $X = 2.5\,m$ (Fig. 1 (d)). Each profile consists in 24 vertical $10\,Hz$ geophones spaced of $30\,cm$ to form a $6.9\,m$ profile in the centre of each $7\,m$-long area. For each profile, seismic shots were obtained using a $1\,kg$ hammer hitting an iron ingot between two adjacent geophones. The first shot was taken at $15\,cm$ offset before the first geophone (1/2 inter-geophone

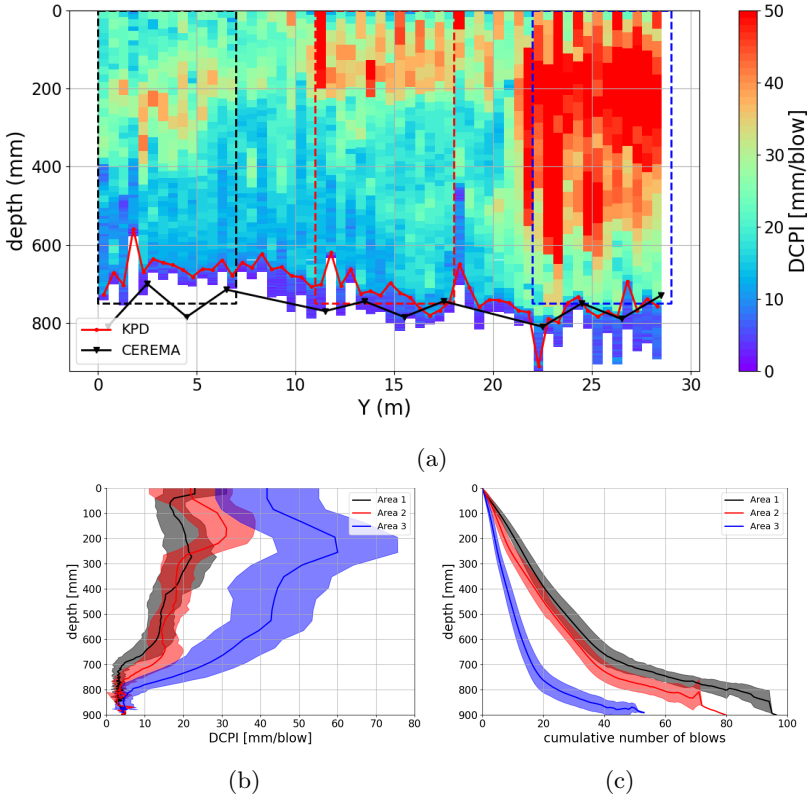

Figure 2: (a) Raw values of $DCPI$ at each measurement position, and the site test thickness estimated by KPD method (red) and measured during the construction (black). (b) Mean and STD values of $DCPI$ as a function of depth. (c) Mean and STD values of the cumulative $DCPI$ in each area as a function of the cumulative number of blows. A number of 140 DCP soundings were used for the calculation of the mean and STD values in each area.

spacing). To improve the signal-to-noise ratio, the recorded data at each shot position were obtained after stacking four hammer impacts. The time length of the recorded data was $2\,s$ with a sampling period of $0.25\,ms$ and a pre-triggering delay of $-0.025\,s$.

The Common Mid-Point Cross-Correlation (CMPCC) method (Hayashi and Suzuki, 2004) was applied to reconstruct high-resolution pseudo-2D cross-sections of V_s, using the software SeisImager (Geometrics Inc.). The CMPCC method, like many other surface-wave methods for the (pseudo-)2D V_s cross-section construction (Bergamo et al., 2012; Pasquet and Bodet, 2017), applies the local 1-D layered Earth hypothesis. Cares must be taken for the parametrization of, e.g. the window size in which the 1D hypothesis is considered with respect to the seismic set-ups and the lateral variation of the site, the number of data stacked in the window, and some classical issues of application of surface-wave methods, such as the mode consideration, the source energy and its frequency range, the inversion parameterization, etc. The picks of the dispersion curves of the fundamental mode are available in Fig. 3, after the data transformation from the $V_{ph} - f$ domain to pseudo-depth ($\lambda/2.5$)-apparent V_s ($V_{ph} \times 1.1$) domain (O'Neill, 2004), with f being the frequency, V_{ph} being the phase velocity, and λ being the wavelength. The lack of dispersion data is observed for the small wavelength (pseudo-depth $< 200\,mm$) because of the poor energy distribution at $f > 200\,Hz$, and for deep medium (pseudo-depth $> 1000\,mm$) owing to the maximum measurable wavelength related to the length of seismic profile (Bodet et al., 2005). The raw seismic data and the details of surface-wave processing and analyses are available in the Supporting Information.

2.3.2 Inversion of surface-wave data

Smooth-model inversion of MASW data has been performed using the 2D Surface-Wave modules in SeisImager (Geometrics), which is based on NLLSM

parameter	value	definition
N_{iter}	10	number of iteration
α	0.15	stabilizers
β	1	
e	0.1	damping factor
r_v	0.5	vertical regularization parameter
r_h	0.5	horizontal regularization parameter

Table 2: Inversion parameters and their values for the inversion of the site test in SeisImager.

approach (Feng and Sugiyama, 2001; Hayashi, 2008). In order to compare the inverted V_s profile with DCP data, initial models were set with 20 layers of $5\,cm$ thickness each. According to the measured V_{ph}, homogeneous models were used as initial models with $V_s = 133\,m/s$ for Area 1, $V_s = 142\,m/s$ for Area 2, and $V_s = 129\,m/s$ for Area 3. The values of V_s corresponds to the mean values of measured $V_{ph} \times 1.1$ in each area. The P-wave velocity $V_p = 500\,m/s$ and the density $\rho = 1800\,kg/m^3$ were fixed in the inversion of which the values are obtained by the seismic refraction analysis and geotechnical measurements on samples. Inversion parameters are available in Table 2.

The inverted V_s (pseudo) cross-sections of three areas by the NLLSM are presented in Fig. 3 (d)-(f). They are coherent with the design of the test site but with inherent variations. V_s variations are observed in Area 1 and Area 2 in both the vertical and horizontal directions: one layer with low V_s ($\approx 120\,m/s$) is observed between $[250, 500]\,mm$ bgs; lateral variations are not significant from $600\,mm$ bgs with $V_s \approx 170\,m/s$. Compared to Area 1 and Area 2, Area 3 shows better homogeneity ($V_s \approx 150\,m/s$) in both the horizontal and lateral directions below the first $200\,mm$. Fig. 3 (g) presents the mean and STD values of the inverted V_s in each area. All three curves show higher STD values for the first $200\,mm$, because of the limitation of dispersion data at $f > 200\,Hz$. At $200 - 450\,mm$ bgs, the V_s spindles overlap, which means that V_s has similar values across the three area, and the lateral variations are significant. Below

450 mm bgs, the similarity of Area 1 and Area 2 is again observed where V_s value increases as function of depth and is separated from that of Area 3.

2.3.3 Seismic data error estimation

In order to obtain accurate errors analysis, a systematic global optimization approach is applied, which is based on the Neighborhood Algorithm (NA) and has been performed with Dinver (Geopsy) open source software (Sambridge, 1999; Wathelet, 2004). Comparing to the 2D NLLSM inversion procedure to extract smooth V_s models at each location, the NA inversion gives the possibility to estimate the error of the corresponding V_s profiles. Defining the parameter space in which the models will be searched pseudo-randomly, the error will be defined as the STD of the selected acceptable models.

The NA inversion of seismic data was performed on each extracted dispersion curve. Each inversion performs 10 identical runs with same parametrization and each run searched 10000 models in the defined parameter space. The acceptable models are the best 10% models in each run with minimum misfit values, which gives 10000 models for each inversion. Based on the inversion results in Fig. 3 (g), 4-layer models were searched with the first three layers representing the test site and the last semi-infinite space representing the fill layer below. The parameter space and inversion setting are available in Table 3. According to the 10000 selected models, the V_s error is defined as the ratio between the STD ($std(V_s)$) and the mean value ($\bar{V_s}$) of the selected models

$$error(V_s) = \frac{std(V_s)}{\bar{V_s}}. \tag{1}$$

The mean V_s values of selected models at each location are presented in Fig. 4 (a), and (b) the associated error sections. Fig. 4 (c) and (d) show the median value of the V_s cross-section in each area, and the boxplots show the

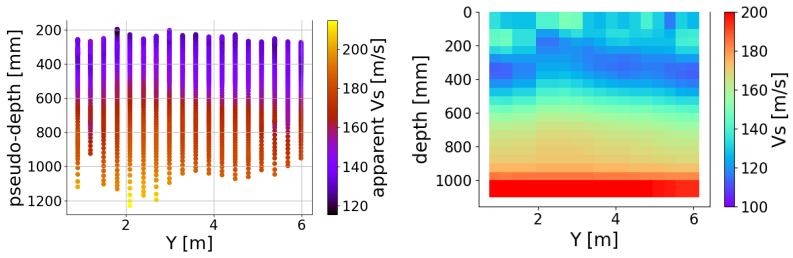

(a) Area 1

(b) Area 1

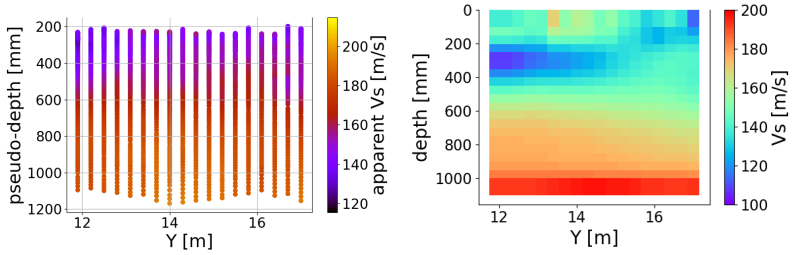

(c) Area 2

(d) Area 2

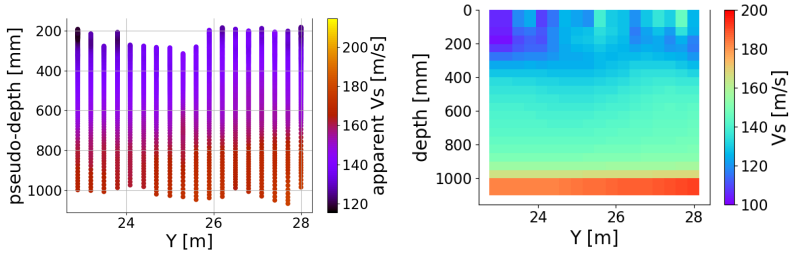

(e) Area 3

(f) Area 3

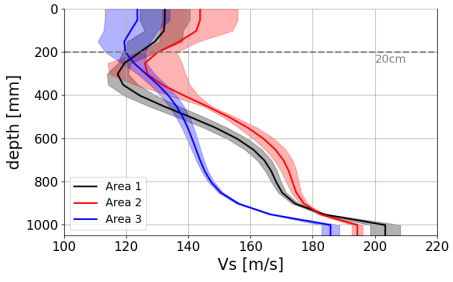

(g)

Figure 3: The picking dispersion curves in pseudo-depth($\lambda/2.5$)-apparent V_s domain in (a) Area 1, (c) Area 2, and (e) Area 3. (b), (d), and (f): Inverted pseudo-2D cross-section of V_s in Area 1 ($RMSE = 2.1\%$), Area 2 ($RMSE = 1.6\%$) , and Area 3 ($RMSE = 1.1\%$). (g): Mean and STD values of V_s in each area. RMSE: Root-Mean-Square Error.

layer	$V_s\,[m/s]$	$V_p\,[m/s]$	$\rho\,[kg/m^3]$	$depth\,[cm]$
1	[50, 200]	[200, 700]	1800	[10, 20]
2	[50, 200]	[200, 700]	1800	[40, 50]
3	[50, 300]	[200, 700]	1800	[60, 100]
4	[100, 300]	[150, 1000]	2000	∞

Table 3: Parameter space settings for the NA inversion. 10 identical runs are performed and each run has the generated models $N_s = 10000$, the initial models $N_{s_0} = 100$, and the best cells $N_r = 100$.

lateral variations in each area at different depth. Due to the lack of information on the high frequencies, all three areas have significant V_s errors (above 15%) in the first layer. In the second layer, the three areas have similar median V_s values, and Area 1 and Area 2 have more significant lateral variations than Area 3. In the third layer, the lateral variations in Area 1 and Area 2 are still more significant than Area 3, but differences are observed between the median values of Area 1&2 and Area 3.

In the following section, V_s cross-sections with smooth inverted models in Fig. 3 (d)-(f) are used as auxiliary variable for the mapping of DCP soundings, and V_s error sections in Fig. 4 (b) are the associated measurement error of the auxiliary variable. Considering the limited resolution for the near-surface and the thickness of the test site, only the inverted V_s values and its associated error in the depth range of $[200, 800]\,mm$ bgs are used.

2.4 Geostatistical workflow

Fig. 5 presents the workflow of the geostatistical study. First, the total number of 58 DCP soundings, placed on the center line ($X = 2.5\,m$) of the test site with $29\,m$ of length and $50\,cm$ of inter-sounding space, were used to generate reference sections, which are considered as the "true" $DCPI$ section of the test site. Then the DCP soundings are decimated progressively, i.e. keep one DCP sounding for every $1\,m$, $1.5\,m$, $2\,m$, ..., $10\,m$. The distance between two

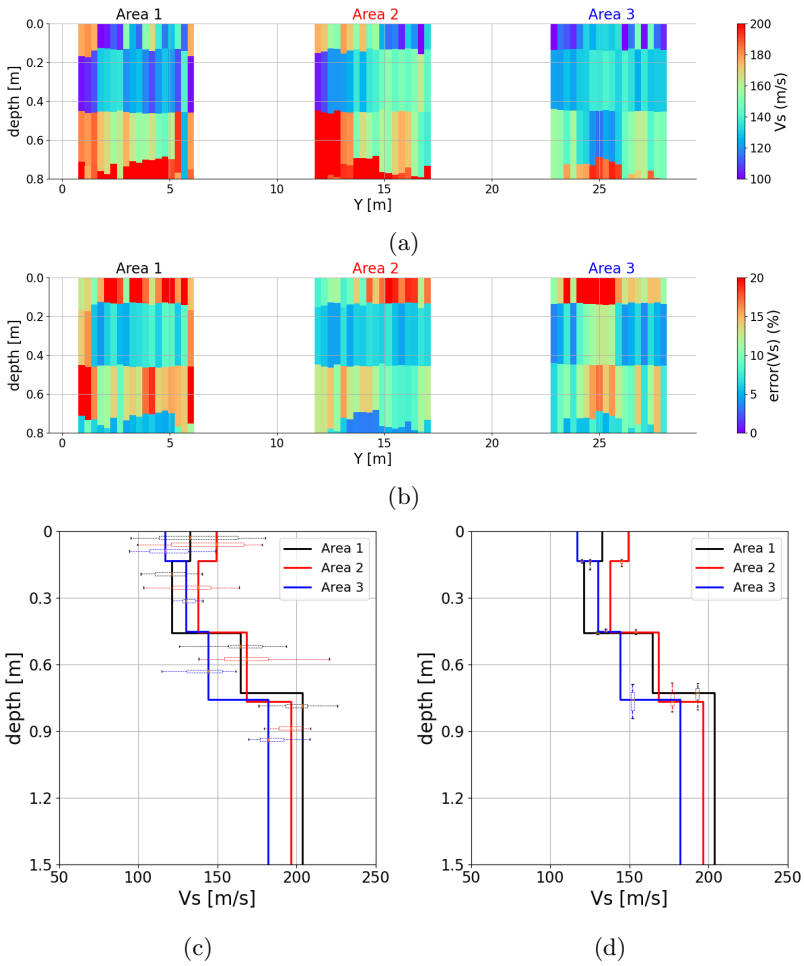

Figure 4: (a) Inverted pseudo-2D cross-section of V_s using NA approach and (b) associated V_s error. Median V_s values in each area are presented as a function of depth with boxplots representing the quantile and extreme values of V_s in (c) and of depth in (d) of each layer. The depth variation of the first and the second layers are less than 1 cm.

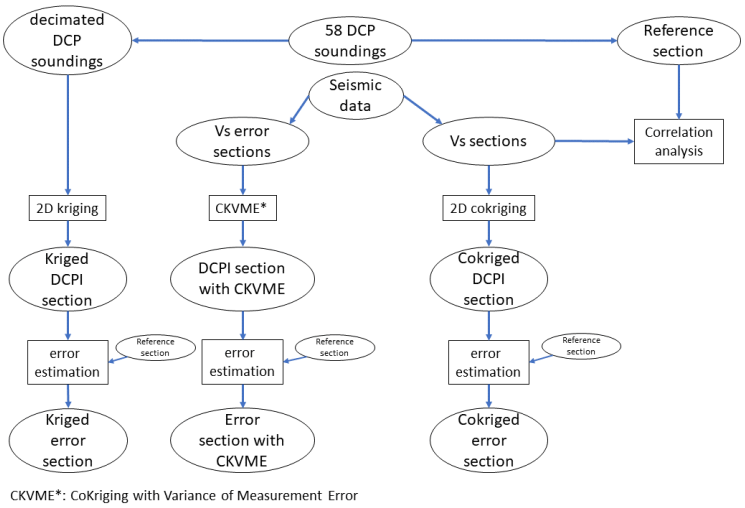

Figure 5: Workflow of the geostatistical study.

adjacent DCP soundings is defined as d_{DCP} hereafter. The remaining DCP soundings were used for the mapping of $DCPI$ at the whole test site scale. Three geostatistical approaches are applied for the mapping of DCP data. The first approach is the ordinary cokriging using $DCPI$ as principal variable and inverted V_s values as auxiliary variable; the second approach is CoKriging with Variance of Measurement Error (CKVME) (Wackernagel, 2003; Christensen, 2011) which introduce the V_s error into the cokriging system; the third method is the ordinary kriging without the use of V_s as auxiliary variable. Finally, the kriging or cokriging sections of $DCPI$ are compared with the reference sections in order to estimate the errors. The geostatistical analyses and calculations were performed using Isatis.neo (Geovariance Inc.).

2.4.1 CoKriging with Variance of Measurement Error

The formulations of kriging with variance of measurement errors can be found in studies such as Wackernagel (2003); Christensen (2011). Considering the measurement errors are available only for the auxiliary variable, the formulations

289 for cokriging are expanded as follows.

Defining $Z(\mathbf{u})$ the principal variable at location $\mathbf{u}$, and the measurable auxiliary variable $Y(\mathbf{u}') = y(\mathbf{u}') + \epsilon(\mathbf{u}')$ at location $\mathbf{u}'$. $y(\mathbf{u}')$ is the intrinsically stationary variable representing the true value that we wish to measure, and $\epsilon(\mathbf{u})$ is its measurement error. By definition, $\epsilon(\mathbf{u})$ is the site-specific zero-mean measurement error and its variance $var(\epsilon_{\mathbf{u}}) = \sigma^2_{\mathbf{u}}$. Moreover, the measurement errors are uncorrelated with principal and auxiliary variables, which means:

$$cov(Z(\mathbf{u_i}), \epsilon(\mathbf{u'_j})) = 0,$$
$$cov(y(\mathbf{u'_i}), \epsilon(\mathbf{u'_j})) = 0,$$

and they are independent, i.e.

$$cov(\epsilon(\mathbf{u'_i}), \epsilon(\mathbf{u'_j})) = 0, \quad \text{if } i \neq j,$$

290 with *cov* being the covariance.

By the ordinary cokriging method (Goovaerts, 1998), the principal variable is estimated as

$$Z^*(\mathbf{u_0}) = \sum_{\alpha} \lambda^Z_{\alpha} Z(\mathbf{u}_{\alpha}) + \sum_{\beta} \lambda^y_{\beta} y(\mathbf{u}_{\beta}), \tag{2}$$

with λ^Z_{α} and λ^y_{β} being the cokriging coefficients for the principal and auxiliary variables. The CKVME system is

$$\begin{bmatrix} \mathbf{C_{ZZ}}(\mathbf{u_i}, \mathbf{u_j}) & \mathbf{C_{Zy}}(\mathbf{u_i}, \mathbf{u'_j}) & \mathbf{1} \\ \mathbf{C_{yZ}}(\mathbf{u'_i}, \mathbf{u_j}) & \mathbf{C_{yy}}(\mathbf{u'_i}, \mathbf{u'_j}) & \mathbf{1} \\ \mathbf{1} & \mathbf{1} & 0 \end{bmatrix} \begin{bmatrix} \mathbf{\Lambda_Z} \\ \mathbf{\Lambda_Y} \\ -\mu \end{bmatrix} = \begin{bmatrix} \mathbf{C_{ZZ}}(\mathbf{u_i}, \mathbf{u_0}) \\ \mathbf{C_{yZ}}(\mathbf{u'_i}, \mathbf{u_0}) \\ 1 \end{bmatrix}, \tag{3}$$

291 where $\mathbf{C_{ZZ}}$, $\mathbf{C_{yy}}$ and $\mathbf{C_{yZ}}$ are covariance and cross-covariance matrix, $\mathbf{\Lambda_Z}$ and
292 $\mathbf{\Lambda_Y}$ are cokriging coefficient vectors, μ is the Lagrange multiplier. The elements

in the covariance and cross-covariance matrix are:

$$C_{ZZ}(\mathbf{u_i}, \mathbf{u_j}) = cov[Z(\mathbf{u_i}), Z(\mathbf{u_j})], \tag{4}$$

$$C_{yy}(\mathbf{u'_i}, \mathbf{u'_j}) = \begin{cases} cov[Y(\mathbf{u'_i}), Y(\mathbf{u'_j})], & \text{if } i \neq j \\ cov[Y(\mathbf{u'_i}), Y(\mathbf{u'_j})] - \sigma^2_{\mathbf{u_i}}, & \text{if } i = j \end{cases}, \tag{5}$$

$$C_{yZ}(\mathbf{u'_i}, \mathbf{u_j}) = cov[Y(\mathbf{u'_i}), Z(\mathbf{u_j})]. \tag{6}$$

With $Z(\mathbf{u})$ representing the principal variable $DCPI$, and $Y(\mathbf{u}')$ being the auxiliary variable V_s, the variance of measurement error $\sigma^2_{\mathbf{u}}$ is $std(V_s)^2$ from the NA inversion in section 2.3.3.

Note that the ordinary kriging and cokriging (without the measurement error) systems are similar to CKVME, which can be found in many literature such as Goovaerts (1998); Wackernagel (2003). Therefore the detailed formulations are not given in this study. The fundamental steps of the three geostatistical approaches are the same: (1) using measured variables to calculate the covariance or cross-covariance matrix on the left-hand of Eq. 2.4.1; (2) fitting theoretical variogram or cross-variogram based on the experimental data and calculate the vector right-hand side of Eq. 2.4.1; (3) resolving Eq. 2.4.1 to obtain kriging or cokriging coefficients and using Eq. 2.4.1 to calculate estimated variables at position $\mathbf{u_0}$.

2.4.2 Error estimation

To estimate the errors of the kriging and cokriging sections, the error section and the $RMSE$ value are calculated regarding to the reference section as follows:

$$error_i = \frac{DCPI_i^{est} - DCPI_i^{ref}}{DCPI_i^{ref}} * 100\%, \tag{7}$$

$$RMSE = \sqrt{\frac{1}{N}\sum_{i}^{N} error_i^2}, \tag{8}$$

where $DCPI_i^{est}$ and $DCPI_i^{ref}$ are estimated and the reference $DCPI$ values at the $i-th$ grid cell, in which i is the grid cell index, and N is the total number of cells of the section of the test site.

3 Results

3.1 Relation between DCP and surface-wave data

In order to analyze the relationship between the DCP and surface-wave data, the measured MASW dispersion data before inversion, apparent V_s, was first compared with the slope of cumulative $DCPI$, S_{DCP}, because both data integrate information from the surface to a given depth. S_{DCP} was estimated by the linear regression method on the cumulative $DCPI$ of each DCP sounding, from the surface to the pseudo-depth of MASW dispersion data. Then the correlation between apparent V_s and S_{DCP} at the same (pseudo-)depth in each area was analyzed and shown in Fig. 6 (a)-(c). Although there is a high degree of similarity between Area 1 and Area 2, Area 2 has a higher correlation coefficient than Area 1, benefiting from higher S_{DCP} values for the first $300\,mm$ and greater DCP penetration depths detected by KPD method. The correlation coefficient equal to -0.34 in Area 3 owing to the highly dispersed S_{DCP} values caused by the strong $DCPI$ variations in the vertical direction.

Fig. 6 (d)-(f) show the relationship between the raw $DCPI$ data and the inverted V_s values with respect to depth. The correlation coefficients of three

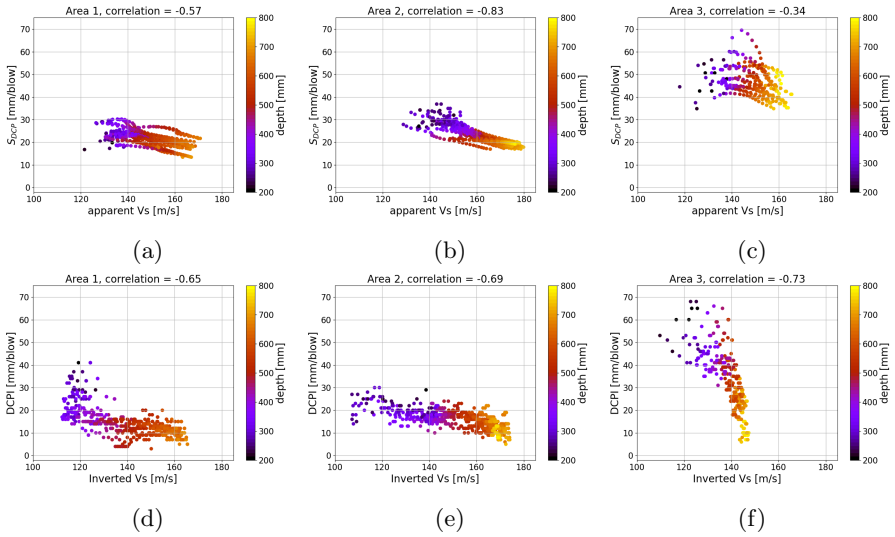

Figure 6: (a)-(c): S_{DCP} and apparent V_s correlation. (d)-(f): $DCPI$ and inverted V_s correlation. The correlation coefficient between two variables X and Y is calculated using formulation $corr = \frac{E[(X-E[X])(Y-E[Y])]}{\sigma_X \sigma_Y}$ with $E[\cdot]$ and σ being the average and the standard deviation values.

areas are close while Area 3 has different pattern compared to the other two areas, because of the dispersed $DCPI$ and smaller range of V_s values.

Fig. 7 estimates the spatial correlation between $DCPI$ and V_s data by calculating the bi-directional experimental variograms and cross-variogram (Gringarten and Deutsch, 2001; Oliver and Webster, 2014), applying the Gaussian anamorphosis (Wackernagel, 2003). The fitted theoretical models are the black solid curves. The nugget effect was not observed in the experimental (cross-)variograms which ensured the spatial correlation and non-randomness in the data (Gringarten and Deutsch, 2001). The spatial correlation decreases as a function of the lag distance despite the slight increasing trend in the $DCPI$ variogram after the sill. This is because of the size of the test site, which is not long enough to show the disappearance of the spatial correlation after the range. Discontinuities are observed in the variogram of V_s and the cross-variogram at $6 - 7\,m$, which are caused by the lack of V_s data in the dead zones; a local peak is observed at a

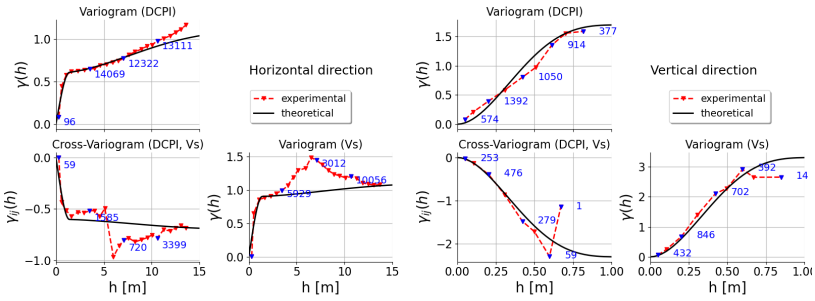

Figure 7: Bi-directional variograms and cross-variogram of $DCPI$ and V_s for the test site. Red triangle: experimental (cross-)variograms; black solid line: theoretical (cross-)variograms. Several triangles are shown in blue with their corresponding number of pairs.

lag of $7\,m$ – size of each area.

3.2 Mapping of DCP soundings

Fig. 8 (a) shows the RMSE values of the three geostatistical methods, as a function of d_{DCP}. When the d_{DCP} increases, the number of remaining DCP soundings used for the mapping decreases (Fig. 8 (b)). The cokriging and CKVME approaches have higher RMSE values when $d_{DCP} < 4.5\,m$. When $d_{DCP} \leq 7.0\,m$, RMSE values of the kriging increase slowly from 19% to 60%. From $d_{DCP} = 7.0\,m$ to $7.5\,m$, the RMSE value of kriging increases sharply by 87%, while the RMSE values increase 25% and 17% for cokriging and CKVME respectively. The use of measurement error in the cokriging system produces slightly smaller RMSE values than without the measurement error.

Fig. 9 shows the $DCPI$ sections using the three methods respectively. For each method, the reference section was obtained using all the 58 DCP soundings; the section 1 was estimated using 29 DCP soundings ($d_{DCP} = 1\,m$); and the section 2 used only three DCP soundings ($d_{DCP} = 10\,m$) and their locations are shown by black dots. Error sections were calculated using Eq. 7. Comparison

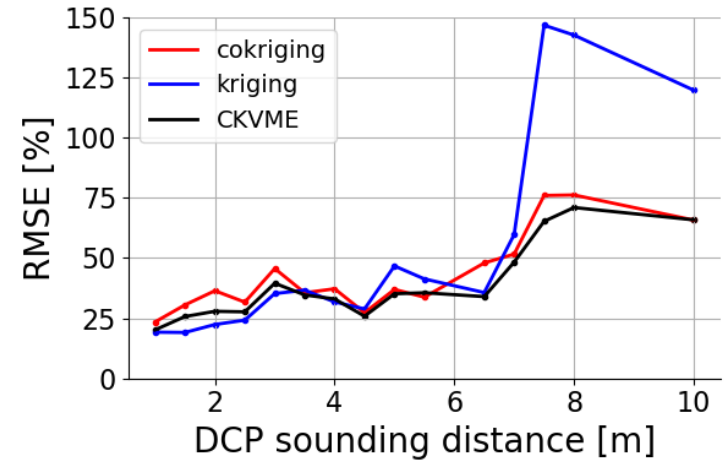

(a)

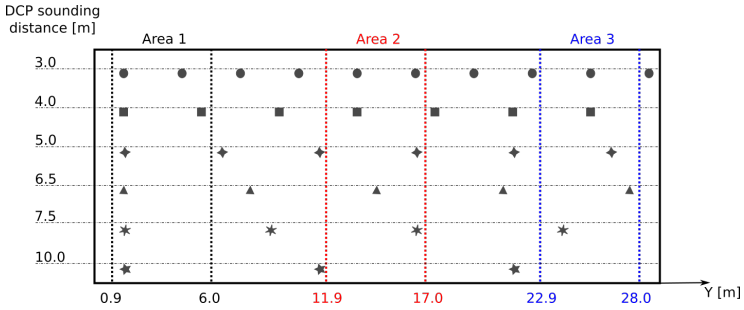

(b)

Figure 8: (a) RMSE curves of kriging, cokriging and CKVME as a function of d_{DCP}. (b) Locations of decimated DCP soundings, using six different d_{DCP} values as example.

of the section 1 for the three methods shows that when no auxiliary variable is introduced, the $DCPI$ sections are smoother and the change in $DCPI$ is continuous. When auxiliary variables are used, $DCPI$ changes become sharper.

When only three DCP soundings are used in the kriging method, the variation of $DCPI$ in the total test site is badly estimated. With the help of auxiliary variable, the cokriging method reduces the RMSE value (65.77%) to almost a half of the kriging method (119.75%), but high errors are observed across the test site. For example, the $DCPI$ values are overestimated in the shallow medium in Area 1 with $error > 40\%$, and underestimated in the deep medium in Area 2 and the entire Area 3 with $error < 40\%$. The section 2 of the CKVME method shows more continuity compared to the cokriging method, and the corresponding errors are reduced inside of all three areas.

4 Discussion

In Fig. 8, the cokriging and CKVME methods show no advantage when $d_{DCP} \leq 7\,m$, i.e. the length of each area. There are several reasons. First, Fig. 9 shows that the kriging method produces smoother and more continuous $DCPI$ section than the cokriging and CKVME methods. With smaller values of d_{DCP}, a large number of DCP soundings are used for the kriging which helps to reduce the error of $DCPI$ sections. Second, at least one DCP sounding is located in each area. Because each area was constructed homogeneously with limited variations, the remaining DCP soundings can roughly represent the $DCPI$ data in each area. Besides, numerous DCP soundings being uniformly distributed in three near-rectangular areas also helps to reduce the kriging errors (Li and Heap, 2008, Chapter 6.1). The above reasons complete each other and together result in the small RMSE values of kriging with $d_{DCP} \leq 7\,m$. Fig. 8 (b) shows that when d_{DCP} varies from $7\,m$ to $7.5\,m$, there is still at least one DCP sounding

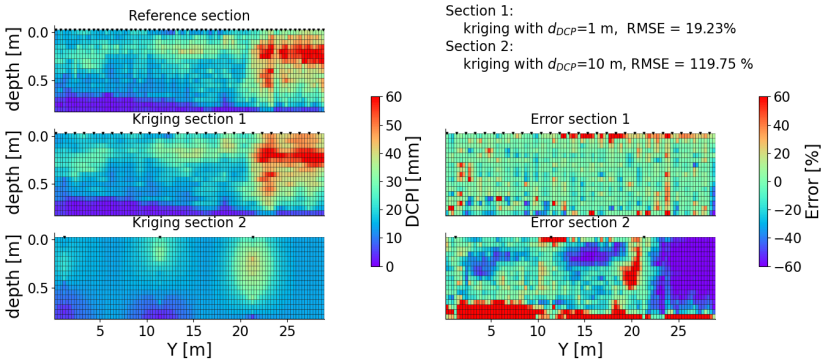

(a)

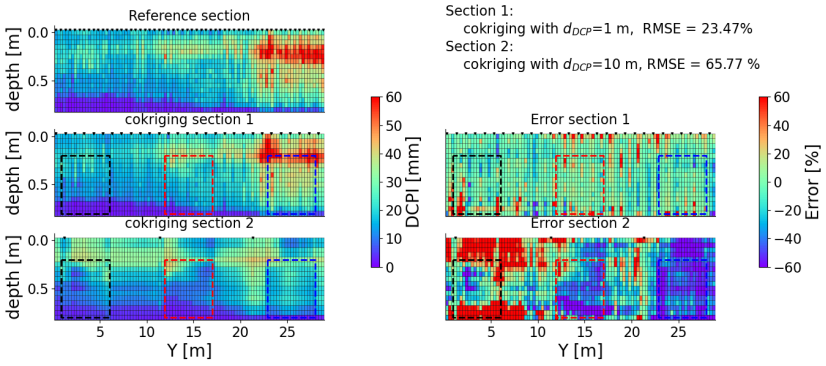

(b)

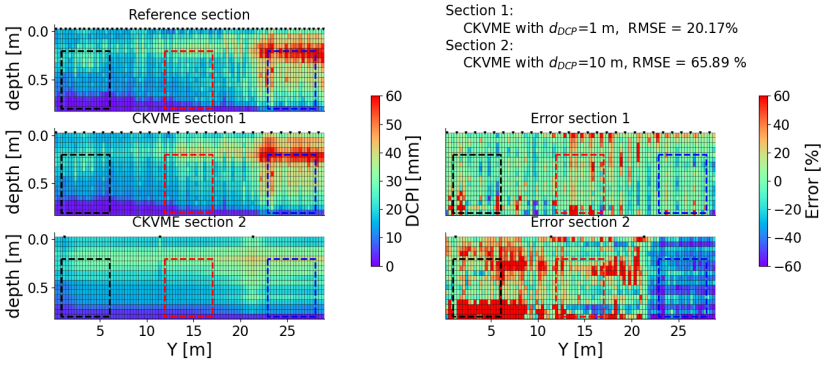

(c)

Figure 9: $DCPI$ and error sections estimated by (a) kriging, (b) cokriging and (c) CKVME methods, using the total 58 DCP soundings (reference section), 29 DCP soundings (section 1, $d_{DCP} = 1\,m$) and 3 DCP soundings (section 2, $d_{DCP} = 10\,m$) respectively. Black triangles: position of DCP soundings. Dashed rectangles: V_s sections referring to Fig. 3.

in each area but the RMSE of kriging method increases sharply. The reason lies in the uneven distribution of DCP sounding locations inside of each area. In summary, the small RMSE values demonstrated by kriging with the data obtained on the test site are not guaranteed in field measurement tests.

From $d_{DCP} = 7.5\,m$, the RMSE values of kriging stay high because the horizontal variability of $DCPI$ cannot be correctly described only with very limited number of DCP soundings. When no or very little *a priori* information is available, any kind of variogram model with any sill value can be used in the kriging system. Depending on the fitted theoretical variogram, the final result of kriging can be completely different and untrustworthy. While introducing the V_s values as auxiliary and physical constrain, the theoretical variogram model in the horizontal direction is constrained by the V_s variability, i.e. the variogram model and sill values of $DCPI$ are fixed by the calculated variogram of V_s. Therefore, the RMSE value still increases with d_{DCP} but not as sharply as the kriging results in Fig. 8 (a).

When $d_{DCP} = 10\,m$, although CKVME produces smooth sections, its corresponding RMSE value is still 66%, mainly due to the high values of error ($|error| > 30\%$) at the bottom of Area 1 and the entire Area 3. This means that, with the constrains of V_s, the lateral variations of $DCPI$ are described, but extreme values, i.e. $DCPI \leq 5\,mm$ at the bottom of Area 1, and $DCPI \geq 40\,mm$ in Area 3, cannot be correctly estimated. Therefore, during field measurements, it is strongly recommended that at least two DCP tests are performed in areas where MASW data show strong variations, either the change of layer depth or the V_s values, in order to obtain the extreme values of $DCPI$ within the areas.

The discontinuity of $DCPI$ variation in the section 2 of cokriging method (Fig. 9 (b)) is caused by the discontinuous V_s sections. By introducing the measurement error in the cokriging system, the CKVME method becomes a

spatial smoother (Christensen, 2011) which gives smaller values of RMSE than the cokriging method in Fig. 8 (b). Cares must be taken on the nugget effect in the variogram and the cross-variogram of CKVME. In general, the nugget effect is affected by the measurement error and the microscale variation. Considering only the variance of measurement error will cause over-smoothed results (Christensen, 2011).

The applied MASW methods are limited to provide high-resolution V_s cross-section at the first $20\,cm$, due to the lack of information at very high frequencies ($f > 200\,Hz$). Using a controlled vibrometer, e.g. a magnetostrictive vibroseis source as in Wawerzinek et al. (2022), is one possible solution to achieve this resolution. Reducing the inter-geophone spacing would be another option, but too small spacing would lead to signal saturation problems. Another issue is the miniaturization of the plate and the source for precise positioning. For these considerations, wireless geophones oe distributed setups such as the fiber optic, e.g.Vantassel et al. (2022), could be tested. However, a compromise should be made between the propagation distance and the required high resolution, because of the high attenuation of the seismic waves at high frequencies (Aki and Richards, 2002). For field measurement, towed land streamer seismic device (Van der Veen and Green, 1998; Pugin et al., 2004) can be used to increase the speed and efficiency. In the cases where a strong lithological contrast or a low-resistant layer between two high-resistant layers is observed in the geotechnical data at shallow depths, the fundamental mode is no more dominant therefore the higher modes of surface-waves should be considered (Foti et al., 2018). The measurement error of the auxiliary variable can also be defined as the *a posteriori* probability density function of the inverted parameter through the application of Bayes' theorem, such as the study of Burzawa et al. (2023) in the application of the railway earthworks.

The variable S_{DCP}, introduced for the observation of acquired DCP data in the test site, is used in geotechnics for the identification of soil layers and their thickness. Examples can be found in the Tri-Service Pavements Working Group Manual TSPWG 3-260-03.02-19, Airfield Pavement Evaluation Standards and Procedures. S_{DCP} calculates the slope of the cumulative $DCPI$ (i.e. the penetration depth of the tip) as a function of the cumulative number of blows, thus integrates information from the top surface to the penetration depth. The variable $DCPI$, however, corresponds to the penetration depth of each blow and provides information of a local area. The use of KPD method can efficiently determine the number of layers and their thickness. Such information can be applied as *a priori* information for the inversion of the in situ geophysical data. As for the apparent V_s, it represents the propagation velocity of surface-waves at different wavelength, whereas the wavelength is directly related to the maximum reachable depth of surface-waves. Therefore the apparent V_s integrates the information of the medium from the top surface to the maximum reachable depth. The comparison between S_{DCP} and apparent V_s in Fig. 6 (a)-(c), proves that it is possible to estimate the correlation between the DCP data and the surface-wave data before inversion. But it should be pointed out that the inversion is necessary to obtain the exact relation between the two data.

5 Conclusion

Seismic surface-wave data, V_s section, is used as auxiliary and physical constrains in this study for the mapping of $DCPI$, by the application of geostatistical methods. The proposed approach is validated on a test site for the first time, which contains three areas with different compaction levels. Seismic and high-density DCP campaigns were performed on the test site, and the mathematical and geostatistical analyses are established on the acquired data in order

to estimate their relationship. Using the high-density DCP tests to produce reference sections of $DCPI$, the kriging and the cokriging methods are both applied for the mapping of decimated number of DCP soundings. Furthermore, the CKVME method is also proposed in order to include the estimated measurement error of the auxiliary variable in the cokriging formulas. The advantage of using V_s values as auxiliary and physical constrains emerges when d_{DCP} increases, because of the constrains of $DCPI$ variations in the lateral direction by V_s. When d_{DCP} is larger than the size of each area ($7\,m$), the kriging method can no more estimate the lateral variation of the test site and the RMSE value of the kriging section increases sharply by 87%. With the constrain of the V_s sections, the cokriging and the CKVME approaches have increasing RMSE values by 25% and 17% respectively. The CKVME approach provides smoother sections than the cokriging method because the latter has abrupt variation sections due to the discontinuous V_s section of each area. When d_{DCP} is too large to ensure at least one DCP sounding in each area, neither of the cokriging nor the CKVME approaches can correctly estimate the extreme values of $DCPI$. Therefore, for the field measurement application, it is recommended to perform at least two DCP tests in the areas where significant variations are observed on the MASW data.

References

Adama, D., Bryson, L. S., and Wang, A. (2023). Airfield suitability assessment from geophysical methods. *Transportation Geotechnics*, 42:101059.

Aki, K. and Richards, P. G. (2002). *Quantitative seismology*.

ASTM D6951 (2009). Standard test method for use of the dynamic cone penetrometer in shallow pavement applications. ASTM International.

Bergamo, P., Boiero, D., and Socco, L. V. (2012). Retrieving 2D structures from surface-wave data by means of space-varying spatial windowing. *Geophysics*, 77(4):EN39–EN51.

Bodet, L., van Wijk, K., Bitri, A., Abraham, O., Côte, P., Grandjean, G., and Leparoux, D. (2005). Surface-wave inversion limitations from laser-doppler physical modeling. *Journal of Environmental & Engineering Geophysics*, 10(2):151–162.

Burzawa, A., Bodet, L., Dhemaied, A., Dangeard, M., Pasquet, S., Vitale, Q., Boisson-Gaboriau, J., and Cui, Y. J. (2023). Detecting mechanical property anomalies along railway earthworks by bayesian appraisal of masw data. *Construction and Building Materials*, 404:133224.

Chiles, J.-P. and Delfiner, P. (2009). *Geostatistics: modeling spatial uncertainty*, volume 497. John Wiley & Sons.

Christensen, W. F. (2011). Filtered kriging for spatial data with heterogeneous measurement error variances. *Biometrics*, 67(3):947–957.

Cosenza, P., Marmet, E., Rejiba, F., Cui, Y. J., Tabbagh, A., and Charlery, Y. (2006). Correlations between geotechnical and electrical data: A case study at garchy in france. *Journal of Applied Geophysics*, 60(3-4):165–178.

Feng, S. and Sugiyama, T.and Yamanaka, H. (2001). Application of sensitivity analysis to array design for microtremor array survey. In *Proceedings of the 104th SEGJ Conference*, pages 35–39.

Foti, S., Hollender, F., Garofalo, F., Albarello, D., Asten, M., Bard, P.-Y., Comina, C., Cornou, C., Cox, B., Di Giulio, G., et al. (2018). Guidelines for the good practice of surface wave analysis: a product of the interpacific project. *Bulletin of Earthquake Engineering*, 16:2367–2420.

Goovaerts, P. (1998). Ordinary cokriging revisited. *Mathematical Geology*, 30(1):21–42.

Gringarten, E. and Deutsch, C. V. (2001). Teacher's aide variogram interpretation and modeling. *Mathematical Geology*, 33(4):507–534.

Haines, S. S., Pidlisecky, A., and Knight, R. (2009). Hydrogeologic structure underlying a recharge pond delineated with shear-wave seismic reflection and cone penetrometer data. *Near Surface Geophysics*, 7(5-6):329–340.

Hayashi, K. (2008). Development of surface-wave methods and its application to site investigations. *Ph.D. dissertation*.

Hayashi, K. and Suzuki, H. (2004). CMP cross-correlation analysis of multichannel surface-wave data. *Exploration Geophysics*, 35(1):7–13.

Huang, J., Zheng, D., Li, D.-Q., Kelly, R., and Sloan, S. W. (2018). Probabilistic characterization of two-dimensional soil profile by integrating cone penetration test (cpt) with multi-channel analysis of surface wave (masw) data. *Canadian Geotechnical Journal*, 55(8):1168–1181.

Li, J. and Heap, A. D. (2008). A review of spatial interpolation methods for environmental scientists.

Masoli, C. A., Petronio, L., Gordini, E., Deponte, M., Boehm, G., Cotterle, D., Romeo, R., Barbagallo, A., Belletti, R., Maffione, S., et al. (2020). Near-shore geophysical and geotechnical investigations in support of the trieste marine terminal extension. *Near Surface Geophysics*, 18(1-Quantitative Geophysical Characterisation of Marine Near-Surface):73–89.

Mayne, P. W. and Rix, G. J. (1995). Correlations between shear wave velocity and cone tip resistance in natural clays. *Soils and foundations*, 35(2):107–110.

Mohammadi, S., Nikoudel, M., Rahimi, H., and Khamehchiyan, M. (2008). Application of the dynamic cone penetrometer (DCP) for determination of the engineering parameters of sandy soils. *Engineering Geology*, 101(3-4):195–203.

Mola-Abasi, H., Dikmen, U., and Shooshpasha, I. (2015). Prediction of shear-wave velocity from cpt data at eskisehir (turkey), using a polynomial model. *Near Surface Geophysics*, 13(2):155–168.

Nazarian, S., Tandon, V., Crain, K., and Yuan, D. (2000). Use of instrumented dynamic cone penetrometer in pavement characterization. *ASTM Special Technical Publication*, 1375:214–230.

Oliver, M. and Webster, R. (2014). A tutorial guide to geostatistics: Computing and modelling variograms and kriging. *Catena*, 113:56–69.

O'Neill, A. (2004). Shear velocity model appraisal in shallow surface wave inversion. In *Symposium on the Application of Geophysics to Engineering and Environmental Problems 2004*, pages 1544–1555. Society of Exploration Geophysicists.

Pasquet, S. and Bodet, L. (2017). Swip: An integrated workflow for surface-wave dispersion inversion and profiling. *Geophysics*, 82(6):WB47–WB61.

Porter, O. (1939). The preparation of subgrades. In *Highway Research Board Proceedings*, volume 18.

Pugin, A. J., Larson, T. H., Sargent, S. L., McBride, J. H., and Bexfield, C. E. (2004). Near-surface mapping using sh-wave and p-wave seismic land-streamer data acquisition in illinois, us. *The Leading Edge*, 23(7):677–682.

Sambridge, M. (1999). Geophysical inversion with a neighbourhood algo-

rithm—ii. appraising the ensemble. *Geophysical Journal International*, 138(3):727–746.

Sastre Jurado, C., Breul, P., Bacconnet, C., and Benz-Navarrete, M. (2021). Probabilistic 3d modelling of shallow soil spatial variability using dynamic cone penetrometer results and a geostatistical method. *Georisk: Assessment and Management of Risk for Engineered Systems and Geohazards*, 15(2):139–151.

Satopaa, V., Albrecht, J., Irwin, D., and Raghavan, B. (2011). Finding a" kneedle" in a haystack: Detecting knee points in system behavior. In *2011 31st international conference on distributed computing systems workshops*, pages 166–171. IEEE.

Socco, L. and Strobbia, C. (2004). Surface-wave method for near-surface characterization: a tutorial. *Near surface geophysics*, 2(4):165–185.

Van der Veen, M. and Green, A. G. (1998). Land streamer for shallow seismic data acquisition: Evaluation of gimbal-mounted geophones. *Geophysics*, 63(4):1408–1413.

Vantassel, J. P., Cox, B. R., Hubbard, P. G., and Yust, M. (2022). Extracting high-resolution, multi-mode surface wave dispersion data from distributed acoustic sensing measurements using the multichannel analysis of surface waves. *Journal of Applied Geophysics*, 205:104776.

Wackernagel, H. (2003). *Multivariate geostatistics: an introduction with applications*. Springer Science & Business Media.

Wathelet (2004). Surface-wave inversion using a direct search algorithm and its application to ambient vibration measurements. *Near Surface Geophysics*, pages 211–221.

589 Wawerzinek, B., Lüth, S., Esefelder, R., Giese, R., and Krawczyk, C. M. (2022).
590 Performance of high-resolution impact and vibration sources for underground
591 seismic exploration of clay formations at the scale of a rock laboratory. *Geo-*
592 *physical Journal International*, 231(3):1750–1766.

593 Webster, S. L., Grau, R. H., and Williams, T. P. (1992). Description and applica-
594 tion of dual mass dynamic cone penetrometer. Technical report, Geotechnical
595 Laboratory (US).

596 Xu, J., Wang, Y., and Zhang, L. (2022). Fusion of geotechnical and geophys-
597 ical data for 2d subsurface site characterization using multi-source bayesian
598 compressive sampling. *Canadian Geotechnical Journal*, 59(10):1756–1773.

date	depth [cm]	VWC [%]
2021/06	13	33.68
	23	36.67
	33	36.45
	48	34.34
	73	36.27
2021/10	13	33.75
	23	37.24
	33	37.25
	48	34.85
	73	37.67

Table A.1: Volumetric water content measured by TDR Soilvue in Area 3. Values in June and October are averaged values for the day(s) where DCP and seismic measurements were occurred.

A Geotechnical data of test site

A TDR (Time-Domain Reflectometer) sensor (SoilVUE10[1]) is buried in Area 3 ($X = 3.5\,m$, $Y = 25\,m$) to monitor the soil variations in time. Four parameters, i.e. volumetric water content (VWC), permitivity, temperature and electric conductivity, are measured at five depths ($13\,cm$, $23\,cm$, $33\,cm$, $48\,cm$ and $73\,cm$) with a measurement frequency every 15 min from Feb. 2021. Table A.1 gives the mean VWC values during DCP measurement in June 2021 and seismic measurement in October 2021.

In order to obtain the soil structure and composition of each area, three soil cores, P1-2, P2-1 and P3-1, ware taken from the boreholes, one for each area. Analyses of specimens are available in Table A.2. Granulometric analysis and the X-ray diffraction analysis on the samples of test site show that the material contains approximately 20% of clay and the rest of mixed feldspar and quartz. Due to the unavailability of some extracted specimens, the number of samples and thickness of the three cores differ. VWC and porosity (ϕ) of specimens are calculated using the following formulas: $VWC = V_{water}/V_{solid} = GWC * \rho_{dry}$

[1] https://www.campbellsci.com/soilvue10

Core	depth [cm]	GWC [%]	VWC [%]	ρ_{dry} $[g/cm^3]$	ϕ
P1-2	18-25	15.6	27.92	1.79	0.33
	25-31	18.4	31.10	1.69	0.36
	43-50	16.5	27.89	1.69	0.36
P2-1	6-10	17.5	30.98	1.77	0.33
	10-14	15.5	26.90	1.74	0.35
	14-18	17.8	31.15	1.75	0.34
	31-35	17.7	30.80	1.74	0.35
	35-39	15.5	26.82	1.73	0.35
	39-43	17.9	30.97	1.73	0.35
	50-54	15.4	26.49	1.72	0.35
	54-59	17.9	30.79	1.72	0.35
	59-63	17.7	29.74	1.68	0.37
P3-1	18-25	14.4	24.48	1.7	0.36
	25-31	18.2	32.40	1.78	0.33
	50-56	17.3	27.85	1.61	0.40

Table A.2: Parameters of specimens for three cores at different depths. GWC: gravimetric water content (m_{water}/m_{dry}); VWC: volumetric water content; ρ_{dry}: dry solid density; ϕ: porosity.

and $\phi = 1 - \rho_{dry}/\rho_{particle}$, with $\rho_{particle} = 2661.4\,kg/m^3$ being the particle density of soil. The average porosity of three areas are 0.35, 0.35 and 0.36 respectively, which gives the highest porosity in Area 3 owing to its lowest compaction level. Besides, variations of water content and porosity between specimens from one core imply that there are possible but not significant vertical variations in each area.

The locations of the soil core and the TDR sensor are available in Fig 1 (c).